Elastostatic Model of a New Hybrid Minimally-Invasive-Surgery Robot

Conference Paper · October 2015

DOI: 10.6567/IFToMM.14TH.WC.OS13.085

4 authors, including:

Tanio K. Tanev
Bulgarian Academy of Sciences
25 PUBLICATIONS **287** CITATIONS
SEE PROFILE

Alessandro Cammarata
University of Catania
51 PUBLICATIONS **486** CITATIONS
SEE PROFILE

Davide Marano
Università degli Studi di Modena e Reggio Emilia
11 PUBLICATIONS **16** CITATIONS
SEE PROFILE

The 14th IFToMM World Congress, Taipei, Taiwan, October 25-30, 2015
DOI Number: 10.6567/IFToMM.14TH.WC.OS13.085

Elastostatic Model of a New Hybrid Minimally-Invasive-Surgery Robot

T. K. Tanev*
Institute of Systems Engineering and Robotics
Bulgarian Academy of Sciences, Bulgaria

A. Cammarata, D. Marano and R. Sinatra †
Department of Industrial Engineering
University of Catania, Italy

Abstract—*In this paper, the elastostatic model of a novel hybrid robot for minimally invasive surgery is presented. The parallel robot has two identical limbs of SPU type and a RRR limb which allows the end-effector to accomplish spherical motion. The robot has three actuated joints for the parallel architecture and one for the translation along the longitudinal axis of the surgical instrument. The parallel manipulator provides remote centre of motion located at the incision point of the patient's body. First, the kinematics is solved in closed-form for the forward and inverse positioning problems, then elastostatic analysis of the parallel manipulator is modelled considering a system of flexible links and rigid bodies connected by means of joints. Local stiffness matrices are derived and finally combined to obtain the global stiffness matrix of the robotic system. Results are compared with those coming from commercial FE software for validation. Positioning and orienting errors due to flexibility are evaluated in order to improve quality in positioning and tracking of trajectories. Finally, some extensions to sensitivity analysis are provided to demonstrate that the elastostatic model can be used to improve the performance of the robot.*

Keywords: minimally invasive surgery (MIS); hybrid manipulator; elastostatics; robot kinematics;

I. Introduction

The minimally invasive technique was adopted in surgical operations in the last two decades of the 20th century. In minimally invasive surgery the instruments and camera are inserted into the human body through small incisions on the abdomen and operated inside the patient's body. Long surgical instruments, held and manoeuvred by surgeon's hands, are used in order to reach the operating area in the abdomen. Thus, the minimally invasive technique could be considered some kind of remote manipulation and the introduction of robots in this field was a logical enhancement to the traditional surgical manipulation. Using robots in the minimally invasive surgery allows filtering the trembling of surgeon's hand and scaling its movements. This implies that the robotic assisted surgery helps to perform more complex surgical procedures with a high accuracy. For that reason, recently, a great amount of research has been carried out and many medical robots have been proposed for use in the minimally invasive surgery. Both serial and parallel manipulators have been developed for surgical applications. The abdomen small incision restricts the motion of the instrument and acts as a pivoting point. Thus, only four degrees of freedom are possible, three rotations around three intersecting axes in the pivoting point and a translation along the longitudinal axis of the surgical tool. In general, this desired motion could be achieved by mechanically restriction or by properly controlling a manipulator with full mobility. This restricted motion in the minimally invasive surgery is best described by the term "Remote Centre-of-Motion"(RCM) [1]. It is a point where one or more rotations are centred and located outside the mechanism itself. RCM can be enforced by different types of mechanisms. Zeus surgical system uses isocentre-based RCM mechanism, which can be described as a "pin-in-ring" joint [2]. Other robotically assisted surgical systems such as da Vinci [3] and BlueDRAGON [4], use parallelograms for RMC mechanism. Another RCM mechanism is based on a spherical mechanism. Both serial and parallel robots with implemented spherical kinematic chains have been proposed for use as surgical robots. Open kinematic chains with spherical mechanism have been suggested for application in minimally invasive surgery [5], [6], [7]. Parallel manipulators with spherical linkages have been also proposed especially for application in laparoscopic surgery [8], [9]. Other interesting parallel manipulators providing RCM and designed for minimally invasive surgery are presented in [10] and [11]. Apart from the mechanical RCM, the so called controllable (programmable) RCM is used in the robots for minimally invasive surgery, as well. Obviously, the general type parallel manipulators used in the robot assisted minimally invasive surgery need to provide programmable RCM. For example, in the parallel manipulator of the Gough-Stewart type developed for minimally invasive surgery, the RCM is provided by the control system (programmable RCM) [12]. Some other parallel mechanisms have been also proposed for application in laparoscopy [13], [14]. A type of hybrid parallel manipulator and its kinematics are presented in [15]. The programmable RCM provides motion flexibility since the robot has redundant degrees of freedom. The drawback of the programmable RCM is the complexity of the robot design and control system which increases the error probability. The mechanical RCM are considered to be more suitable for the robotic assisted minimally invasive surgery,

*tanev_tk@hotmail.com
†acamma@di.unict.it, davide.marano@gmail.com, rsinatra@dii.unict.it

due to the fewer degrees of freedom, simpler control system and safer manipulation. The robots providing mechanical RCM are usually rigid, cost-effective and easy controllable. The serial and parallel spherical manipulators provide exact spherical movement at the incision point. The drawback for a parallel spherical manipulator is the requirement for precise manufacturing and alignment of the joints, and also the possibility of clogging.

The process of the robot design includes the determination of the elastostatic properties. The established elastostatic model allows the designer to analyse different options of the robot with various design parameters.

In this paper, the kinematic and elastostatic model of a novel hybrid robot consisting of a parallel manipulator and an additional translational joint attached to the moving platform is presented. This robot, firstly proposed in [16], possesses the ability of the spherical linkage to provide remote centre of motion and overcomes some drawbacks of the parallel spherical manipulators, such as a possible clogging and bulky structure. The stiffness of the robot is modelled and the elastostatic model is developed and presented, which represents the main point of this work. The proposed model is compared to Ansys© to validate results. The error positioning analysis is evaluated for the boundaries of different constant orientation workspaces. The values of linear and angular displacements due to deformation are compared with limit values coming from the medical literature. Finally, we propose some extensions to sensitivity analysis to demonstrate that the proposed elastostatic model can improve the performance of the robot in terms of precision limiting the deformations due to static wrenches acting upon its surgical tool.

II. Robot Kinematics

The considered novel hybrid robot consists of a parallel manipulator and an additional translational joint attached to the moving platform [16]. A CAD model of the considered hybrid robot is shown in Fig. 1. The parallel manipulator provides RCM of the end-effector and the RCM is at the incision point of the patient's body. The hybrid robot has four degrees of freedom, three for the parallel manipulator and a fourth degree of freedom (a translation along the longitudinal axis of the surgical instrument) is provided by an additional prismatic joint attached to the moving platform.

A. Kinematic Scheme of the Robot

The parallel manipulator consists of three limbs, two of them (A_1B_1 and A_2B_2) have identical SPU (spherical-prismatic-universal) joints structure and the third (A_3B_3) is a RRR spherical linkage, i.e. the axes of all three revolute joints (R) of this limb intersect in a single point (Fig. 2). Each limb has one driven joint, respectively. The prismatic joints of the SPU limbs and the second (middle) revolute joint of the RRR limb are driven. In addition to these three active joints for the parallel mechanism, an active prismatic

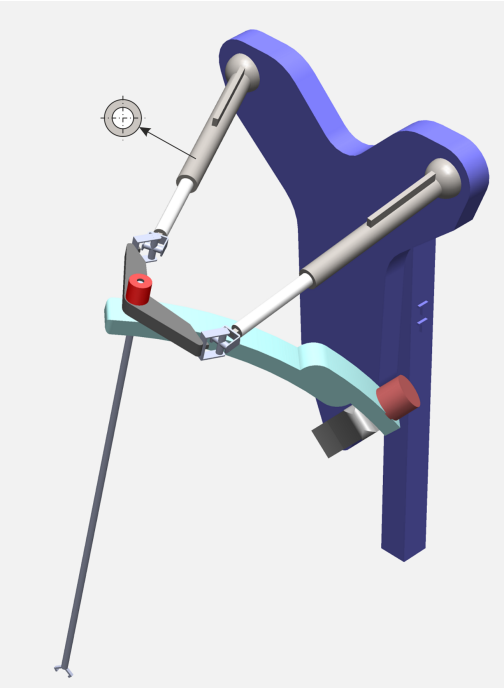

Fig. 1. A CAD model of the minimally-invasive-surgery parallel robot with non-identical limbs.

joint allowing translation of the end-effector along the line OB_3 is added. The axis of the revolute joint (A_3), attached to the base platform (BP), is perpendicular to the plane of the base platform ($A_1A_2A_3$) and the axis of the revolute joint (B_3), attached to the moving platform (MP), is perpendicular to the plane of the moving platform ($B_1B_2B_3$). The origins of the reference (base) coordinate system OXYZ and the coordinate systems $\{1\}$, $\{2\}$ and $\{3\}$ coincide with the intersection point of the three axes of the revolute joints of the spherical RRR limb. The Z_i-axes ($i = 1, 2, 3$) are along the axes of the three revolute joints, respectively. The $O_4X_4Y_4Z_4$ coordinate system is attached to the MP and Z_4-axis is along the direction of translation of the last prismatic joint. The angles of rotation (θ_1, θ_2, and θ_3) about the three Z_i ($i = 1, 2, 3$) -axes are chosen for parameters for kinematic modelling of the parallel mechanism. Using the D-H (Denavit-Hartenberg) notation, the transformation of the coordinate systems can be written as a product of the following rotation (R) and translation (T) matrices

$$\mathbf{Q}_i = R(\alpha_{i-1})T(a_{i-1})R(\theta_i)T(d_i) \tag{1}$$

Then, the transformation matrix $\mathbf{Q}_i$ can be written as

$$\mathbf{Q}_i = \begin{bmatrix} C\theta_i & -S\theta_i & 0 & a_{i-1} \\ C\alpha_{i-1}S\theta_i & C\alpha_{i-1}C\theta_i & -S\alpha_{i-1} & -d_iS\alpha_{i-1} \\ S\alpha_{i-1}S\theta_i & S\alpha_{i-1}C\theta_i & C\alpha_{i-1} & d_iC\alpha_{i-1} \\ 0 & 0 & 0 & 1 \end{bmatrix},$$

where $C\theta_i = \cos\theta_i$; $S\theta_i = \sin\theta_i$; $C\alpha_{i-1} = \cos\alpha_{i-1}$;

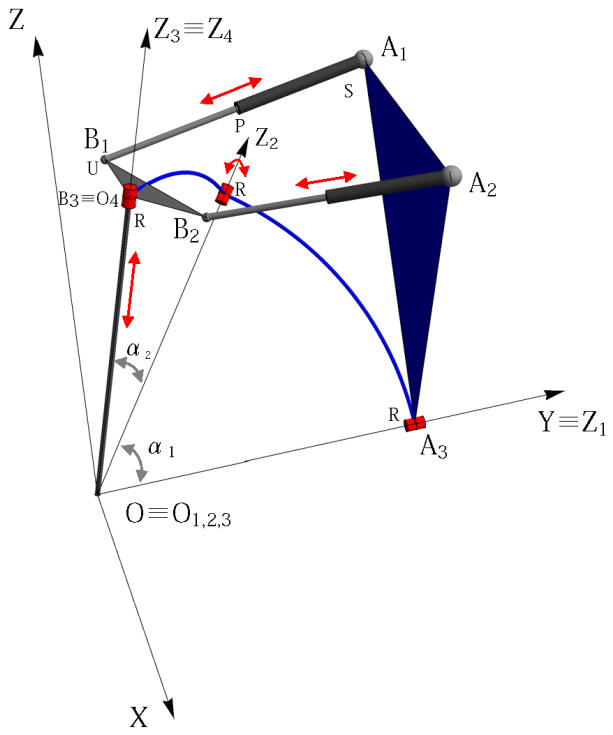

Fig. 2. Kinematic scheme of the manipulator.

i	α_{i-1}	a_{i-1}	d_i	θ_i
1	-$\pi/2$	0	0	θ_1
2	α_1	0	0	θ_2
3	α_2	0	0	θ_3
4	0	0	d_4	0

TABLE I. D-H Parameters

$S\alpha_{i-1} = \sin\alpha_{i-1}$.

The D-H parameters are given in Table I, where α_1, α_2, d_4 are constant design parameters and θ_1, θ_2, θ_3 are joint variables (α_i is the twist angle between two adjacent joint axes, and it is required to rotate the Z_i axis into alignment with the Z_{i+1} axis about the positive X_i axis according to the right-hand rule; $d_4 = \|\mathbf{OO}_4\|$).

Then, the transformation matrix for the considered robot manipulator can be written as follows:

$$\mathbf{Q} = \mathbf{Q}_1\mathbf{Q}_2\mathbf{Q}_3\mathbf{Q}_4 \tag{2}$$

B. Forward Kinematic Problem

The forward position problem for the parallel manipulator is presented briefly here, since more details can be found in [16]. This problem can be resolved using the following constrained equations:

$$L_i = \|\mathbf{OA}_i - \mathbf{OB}_i\|,\ i = 1, 2, \tag{3}$$

where $\|...\|$ denotes the Euclidean norm; $\mathbf{OB}_i = \mathbf{Q}\cdot(\mathbf{O_4B}_i)$; $\mathbf{O_4B}_i$ is a vector given in the $O_4X_4Y_4Z_4$ coordinate system. The vectors $\mathbf{OA}_i$ and $\mathbf{O_4B}_i$, which are determined by the design of the manipulator, are as follows:

$$\begin{aligned}
\mathbf{OA}_1 &= (-x_A, y_A, z_A, 1)^T;\\
\mathbf{OA}_2 &= (x_A, y_A, z_A, 1)^T;\\
\mathbf{OA}_3 &= (0, y_A, 0, 1)^T;\\
\mathbf{O_4B}_1 &= (-x_B, y_B, 0, 1)^T;\\
\mathbf{O_4B}_2 &= (x_B, y_B, 0, 1)^T;\\
\mathbf{O_4B}_3 &= (0, 0, 0, 1)^T.
\end{aligned}$$

Expanding Eq. (3) leads to the following equations:

$$\mathbf{OA}_1^2 + \mathbf{OB}_1^2 - 2\mathbf{OB}_1^T\mathbf{OA}_1 - L_1^2 = 0 \tag{4}$$
$$\mathbf{OA}_2^2 + \mathbf{OB}_2^2 - 2\mathbf{OB}_2^T\mathbf{OA}_2 - L_2^2 = 0 \tag{5}$$

The two leg lengths (L_1 and L_2) and the angle θ_2 are the given parameters for the forward problem of the parallel mechanism. One might observe that the fourth parameter, the translation along the O_4Z_4, is also given, but in this case it is not of significant importance for determining the forward position problem of the parallel manipulator. Expanding Eqs. (4) and (5) we get the following two equations for the unknown variables θ_1 and θ_3:

$$\begin{aligned}
&p_{i1}c_1c_3 + p_{i2}c_1s_3 + p_{i3}s_1c_3 + p_{i4}s_1s_3 \\
&+p_{i5}c_1 + p_{i6}s_1 + p_{i7}c_3 + p_{i8}s_3 + p_{i9} = 0,
\end{aligned} \tag{6}$$

where $c_i = \cos\theta_i$, $s_i = \sin\theta_i$ (i=1,2);
$p_{i1}, p_{i2}, \ldots, p_{i9}$ (i=1,2) are coefficients which are determined by the design and input parameters. Because of the limited space of the paper they are not listed here.

Substituting $\sin\theta_i$ and $\cos\theta_i$ i=1,3 with the tangent-half formulas in Eq. (6) we get two equations in two unknowns. An eight-order polynomial in one unknown is obtained after elimination of one of these two unknowns [16].

C. Inverse Kinematic Problem

Due to the specific structure of the manipulator, the position of the end-effector determines the unit vector along the O_3Z_3 (O_4Z_4, respectively) axis, which is actually the third column of the transformation matrix $\mathbf{Q} = [q_{ij}]$, i=1,...,4; j=1,...,4. Let $\mathbf{p} = [p_x, p_y, p_z]^T$ be a position vector of a point of the end-effector, which lies on the O_4Z_4 axis. Then the unit vector along the O_4Z_4 axis is:

$$\mathbf{u}_p = \frac{-\mathbf{p}}{\sqrt{p_x^2 + p_y^2 + p_z^2}}$$

Actually, this unit vector represents the third column of the rotation matrix. In order to completely construct the transformation matrix **Q** another component has to be given. In this case, the angle ψ between the projection of the O_4X_4 axis on the XY plane and OX axis is specified. There are several ways to construct the orientation matrix. Here, we use the Z-Y-Z Euler angles and in this case the rotation matrix can be written as

$$\mathbf{R} = Rot_Z(\phi)Rot_Y(\beta)Rot_Z(\delta) \tag{7}$$

or

$$\mathbf{R} = \begin{bmatrix} C_\phi C_\beta C_\delta - S_\phi S_\delta & -C_\phi C_\beta S_\delta - S_\phi C_\delta & C_\phi S_\beta \\ S_\phi C_\beta C_\delta + C_\phi S_\delta & -S_\phi C_\beta S_\delta + C_\phi C_\delta & S_\phi S_\beta \\ -S_\beta C_\delta & S_\beta S_\delta & C_\beta \end{bmatrix},$$

where S and C stand for sin and cos, respectively, for the angles given as subscripts;

For the inverse problem, the given parameters are the third column of the orientation matrix $[q_{13}\ q_{23}\ q_{33}]^T$ and the angle ψ, therefore, the orientation matrix needs to be constructed. Then, the angles ϕ and β can be obtained from the third column of the orientation matrix:

$$\phi = \arctan\left(\frac{q_{23}}{q_{13}}\right),$$

$$\beta = \text{Atan2}\left(q_{13}\cos\phi\ + q_{23}\sin\phi, q_{33}\right).$$

Now, considering the given angle ψ between the projection of the O_4X_4 axis on the XY plane and OX axis, the following two equations for the unknown angle δ can be written

$$R_{11} - \sqrt{1 - R_{31}^2}\cos\psi = 0,$$

$$R_{21} - \sqrt{1 - R_{31}^2}\sin\psi = 0,$$

where R_{11}, R_{21} and R_{31} are components of the orientation matrix **R** (Eq.7).

Solving the above two equations together we obtain:

$$\delta = \text{Atan2}\left(M, N\right),$$

where

$$M = -\sin\alpha\cos\psi + \sin\psi\cos\alpha;$$
$$N = \frac{\sin\psi\sin\alpha + \cos\alpha\cos\psi}{\cos\beta}.$$

The coordinates of the origin (p. O_4) of the coordinate system $O_4X_4Y_4Z_4$ can be obtained as:

$$\mathbf{OO}_4 = y_A \cdot \mathbf{u}_p.$$

Then, the transformation matrix **Q** can be completed. Now, the leg lengths L_1 and L_2 directly comes from Eq.(3). The third driven parameter θ_2 is obtained from the following equation:

$$\theta_2 = \pm\text{Atan2}\left(\sqrt{1 - D^2}, D\right)$$

where

$$D = \frac{(\cos\alpha_1\cos\alpha_2 - q_{23})}{\sin\alpha_1\sin\alpha_2}.$$

This completes the solution of the inverse problem. Obtaining the value of the fourth driven parameter, i.e., the translation along O_4X_4 axis is trivial and straightforward. In addition to the above- mentioned solution of the inverse problem, it is useful to get the remaining two joint angles θ_1 and θ_3 in order to determine the configuration of the robot. From the expressions of q_{13} and q_{33} in Eq. (2) the following formula for the angle θ_1 is derived:

$$\theta_1 = \text{Atan2}\left(-k_1q_{33} + k_2q_{13}, k_1q_{13} + k_2q_{33}\right),$$

where $k_1 = \sin\alpha_2\sin\theta_2$; $k_2 = \cos\alpha_1\sin\alpha_2\cos\theta_2 + \sin\alpha_1\cos\alpha_2$.
Similarly, the angle θ_3 can be obtained from q_{11} and q_{21} of Eq. 2, i.e. $\theta_3 = \text{Atan2}\left(k_3V, k_3W\right)$, where: $k_3 = \frac{1}{S\theta_1S\theta_2S\alpha_2 - C\alpha_1S\alpha_2C\theta_1C\theta_2 - S\alpha_1C\alpha_2C\theta_1}$;

$$V = (S\alpha_1S\theta_2)q_{11} + (S\theta_1S\theta_2C\alpha_1 - C\theta_1C\theta_2)q_{21}$$
$$W = (-S\alpha_1C\alpha_2C\theta_2 - C\alpha_1S\alpha_2)q_{11} +$$
$$(-C\alpha_1C\alpha_2S\theta_1C\theta_2 - C\alpha_2C\theta_1S\theta_2 + S\alpha_1S\alpha_2S\theta_1)q_{21}$$

where S and C denote *sin* and *cos* of the corresponding angle.

Using the derived solutions of the inverse position problem, the boundaries of the workspace with constant orientations are obtained for this hybrid robot in [16]. These boundary curves are used in the numerical examples for the elastostatic model of the robot in the next sections of the current paper. Being boundary curves, it should be pointed out that they cross singularity. Singularity analysis of this robot is presented in [17], where the geometric condition for singularity has been obtained. This geometric condition leads to the derivation of the algebraic formulation of the singularity surface of the robot. The singularities within the workspace of the robot are shown ([17]).

The boundaries of the workspace are obtained for the following design parameters:
$\mathbf{OA}_1 = (-0.20, 0.52, 0.56)^T$; $\mathbf{OA}_2 = (0.20, 0.52, 0.56)^T$; $\mathbf{OA}_3 = (0, 0.52, 0)^T$; $\mathbf{O_4B}_1 = (-0.1075, 0.05, 0)^T$; $\mathbf{O_4B}_2 = (0.1075, 0.05, 0)^T$; $\mathbf{O_4B}_3 = (0, 0, 0)^T$; $\alpha_1 = 55^o$; $\alpha_2 = 43^o$; $d_4 = 0.52$ m. The following constraints on the motion are imposed in the workspace derivation: $L_{min} = 0.30$ m; $L_{max} = 0.58$ m (minimum and maximum lengths of the SPU limbs); minimum angle between each SPU limb and the plane of the base platform = 30^o.

III. Nodal displacements and joint-matrices

To describe the elastostatic model of the robot we use a linear formulation developed by Cammarata [18], based on small displacements and Euler angles. For the robot in exam we employ 3D straight Euler beams and 3D curved Timoshenko beams.

Before introducing the stiffness model of the robot a brief mathematical background is first recalled. A nodal displacement array is a six-dimensional array with three translational and three rotational displacements: $\mathbf{u} = \begin{bmatrix} u_x & u_y & u_z & u_\varphi & u_\theta & u_\psi \end{bmatrix}^T$.

Joints introduce kinematic constraints between two consecutive links. When FE are used to model links joint constraints must be rewritten in terms of constraint equations between adjacent nodes. In particular, considering two nodes, belonging to two consecutive links bonded by a joint, it is possible to express the kinematic constraint provided by the joint through an equation among displacements: i.e.,

$$\mathbf{u}_1^2 = \mathbf{u}_2^1 + \mathbf{H}\boldsymbol{\theta} \tag{8}$$

in which subscripts of nodal displacements are referred to the link, while superscripts refer to one of the two end-nodes of the link. The joint-matrix $\mathbf{H}$ and the array $\boldsymbol{\theta}$ depend on the joint type: the former containing unit vectors indicating geometric axes, the latter including joint displacements and rotations.

Here, we recall the joint-matrices necessary to study the kinematic chains of the robot:

Revolute joint:

$$\mathbf{h}^R = \begin{bmatrix} \mathbf{0} \\ \mathbf{e} \end{bmatrix}, \quad \theta^R = \theta \tag{9}$$

where $\mathbf{e}$ is the unit vector along the axis of the revolute joint R and θ is the angle of rotation about the said axis.

Universal joint:

$$\mathbf{H}^U = \begin{bmatrix} \mathbf{0} & \mathbf{0} \\ \mathbf{e}^1 & \mathbf{e}^2 \end{bmatrix}, \quad \boldsymbol{\theta}^U = \begin{bmatrix} \theta^1 \\ \theta^2 \end{bmatrix} \tag{10}$$

where $\mathbf{e}^1$ and $\mathbf{e}^2$ are the unit vectors along the axes of the universal joint U and θ^1 and θ^2 are the angles of rotation about the axes of U.

Spherical joint:

$$\mathbf{H}^S = \begin{bmatrix} \mathbf{0} & \mathbf{0} & \mathbf{0} \\ \mathbf{e}^1 & \mathbf{e}^2 & \mathbf{e}^3 \end{bmatrix}, \quad \boldsymbol{\theta}^S = \begin{bmatrix} \theta^1 \\ \theta^2 \\ \theta^3 \end{bmatrix} \tag{11}$$

where $\mathbf{e}^1$, $\mathbf{e}^2$ and $\mathbf{e}^3$ are the unit vectors along the axes of the spherical joint S and θ^1, θ^2, and θ^3 are the angles of rotation about the axes of S.

The described constraint equations are used to consider joints contribute to elastodynamics in a direct way, without using Lagrangian multipliers to introduce joint constraints.

IV. Stiffness matrix determination

A. Rigid body - flexible body

The 12×12 stiffness matrix $\mathbf{K}_a$ of a rigid body connected to a flexible body by means of a joint, with joint-matrix $\mathbf{H}$, has been obtained in [18]. Here, we recall its final expression:

$$\mathbf{K}_a = \begin{bmatrix} \mathbf{X}^1 & \mathbf{X}^2 \\ \mathbf{O} & \mathbf{1} \end{bmatrix}^T \begin{bmatrix} \mathbf{K}_2^{1,1} & \mathbf{K}_2^{1,2} \\ \mathbf{K}_2^{2,1} & \mathbf{K}_2^{2,2} \end{bmatrix} \begin{bmatrix} \mathbf{X}^1 & \mathbf{X}^2 \\ \mathbf{O} & \mathbf{1} \end{bmatrix} \tag{12}$$

where

$$\mathbf{X}^1 = \mathbf{G} + \mathbf{H}\mathbf{Y}^1 \tag{13a}$$
$$\mathbf{X}^2 = \mathbf{H}\mathbf{Y}^2 \tag{13b}$$
$$\mathbf{Y}^1 = -(\mathbf{H}^T\mathbf{K}_2^{1,1}\mathbf{H})^{-1}\mathbf{H}^T\mathbf{K}_2^{1,1}\mathbf{G} \tag{13c}$$
$$\mathbf{Y}^2 = -(\mathbf{H}^T\mathbf{K}_2^{1,1}\mathbf{H})^{-1}\mathbf{H}^T\mathbf{K}_2^{1,2} \tag{13d}$$

The matrix $\mathbf{K}_2$ is the stiffness matrix of the flexible body while the matrix $\mathbf{G}$ expresses the rigid-body-displacement of the node located at the joint position in terms of a reference node of the rigid body, i.e.,

$$\mathbf{G} = \begin{bmatrix} \mathbf{1} & -\mathbf{D} \\ \mathbf{O} & \mathbf{1} \end{bmatrix} \tag{14}$$

where $\mathbf{1}$ and $\mathbf{O}$, respectively, are the 3×3 identity- and zero-matrices and $\mathbf{D}$ is the Cross-Product Matrix of the vector $\mathbf{d}$ pointing from the reference node towards the joint node.

B. Flexible body - Rigid body

The dual counterpart of the previous case is the connection between a flexible and a rigid body through a joint. The 12×12 stiffness matrix $\mathbf{K}_c$ is briefly recalled from [18]:

$$\mathbf{K}_c = \begin{bmatrix} \mathbf{1} & \mathbf{O} \\ \mathbf{X}^1 & \mathbf{X}^2 \end{bmatrix}^T \begin{bmatrix} \mathbf{K}_1^{1,1} & \mathbf{K}_1^{1,2} \\ \mathbf{K}_1^{2,1} & \mathbf{K}_1^{2,2} \end{bmatrix} \begin{bmatrix} \mathbf{1} & \mathbf{O} \\ \mathbf{X}^1 & \mathbf{X}^2 \end{bmatrix} \tag{15}$$

where

$$\mathbf{X}^1 = \mathbf{H}\mathbf{Y}^1 \tag{16a}$$
$$\mathbf{X}^2 = \mathbf{G} + \mathbf{H}\mathbf{Y}^2 \tag{16b}$$
$$\mathbf{Y}^1 = -(\mathbf{H}^T\mathbf{K}_1^{2,2}\mathbf{H})^{-1}\mathbf{H}^T\mathbf{K}_1^{2,1} \tag{16c}$$
$$\mathbf{Y}^2 = -(\mathbf{H}^T\mathbf{K}_1^{2,2}\mathbf{H})^{-1}\mathbf{H}^T\mathbf{K}_1^{2,2}\mathbf{G} \tag{16d}$$

with the same notation as before.

V. Stiffness analysis

The results of the previous section are used to achieve the generalized stiffness matrices of the three limbs composing the parallel architecture of the robot.

A. Limb $S\underline{P}U$

Referring to Fig. 1, each limb of type $S\underline{P}U$ can be thought as the combination, through a spherical joint S, of the rigid BP to the flexible proximal link, the latter in

turn being coupled to the distal link by the actuated prismatic joint P. Finally, the distal link is connected to the rigid MP through a universal joint U. Considering the actuated P locked at a given elongation, the serial connection of proximal and distal links can be substituted by three beams with different sections and lengths and with stiffness matrices $\mathbf{K}_{ij}$, where i denotes the limb number and j refers to one of the three parts in which a limb is divided for the stiffness analysis. Starting from the base and referring to the section of the prismatic joints shown in Fig. 1, the first beam has a hollow circular section with outer and inner diameters respectively equal to those of the proximal and distal links. The rigid-flexible connection between the beam and the BP can be modeled using the case *rigid body-flexible body* of the previous section. The generalized matrix $\mathbf{K}_{ai}(\mathbf{H}^{S_i}, \mathbf{G}_{A_i}, \mathbf{K}_{i1})$ that we obtain depends on: the joint-matrix $\mathbf{H}^{S_i}$ of the spherical joint at point A_i, the rigid-body-displacement matrix $\mathbf{G}_{A_i}$ and the stiffness matrix $\mathbf{K}_{i1}$ of the first beam. For computational purposes it is convenient to choose $\mathbf{G}_{A_i} \equiv \mathbf{1}_6$, meaning that the reference point of the base is set at point A_i. The second beam is clamped to the first and third beam at its extremities. Its cross section is circular with diameter equal to that of the proximal link.

Finally, the third beam has a circular cross section with diameter equal to that of the distal link and it is clamped to the second beam at one extremity and to the MP at the other extremity through a universal joint at point B_i. The *flexible body-rigid body* case can be employed obtaining a stiffness matrix $\mathbf{K}_{ci}(\mathbf{H}^{U_i}, \mathbf{G}_{B_i}, \mathbf{K}_{i3})$ depending on the joint-matrix $\mathbf{H}^{U_i}$ of the universal joint at point B_i and on the rigid-body-displacement matrix $\mathbf{G}_{B_i}$. The latter is built considering the reference node of the MP at point B_3.

B. Limb $\hat{R}\hat{R}\hat{R}$

The third limb of the robot provides a spherical motion to the end-effector; it is composed of two curved links joined by revolute joints with intersecting axes at the common origin O. In order to find the generalized stiffness matrix of the limb, we use curved beams. Here, we employ the model of Choi and Lim describing a two-node Timoshenko's beam with constant strain fields [19]. The method is based on elements with strain functions assumed independently in order to avoid locking phenomena. Similar formulation, based on modified isoparametric elements can be found in the works of Prathap *et al.* [20] or Palaninathan *et al.* [21].

Let us briefly recall the mathematical background needed to obtain the stiffness matrix $\mathbf{K}_p$ of a curved beam into its local frame; the reader is referred to [19] for a complete description. Given a beam of mean radius R, cross-section area A, Young's modulus E, shear modulus G, shear correction factor β^2 and moments of inertia I_x, I_y and I_z as referred to the local curvilinear coordinate system $x_i - z_i$ shown in Fig. 3, we can express the stress-strain relations by means of the matrix $\mathbf{D}_s$, defined as

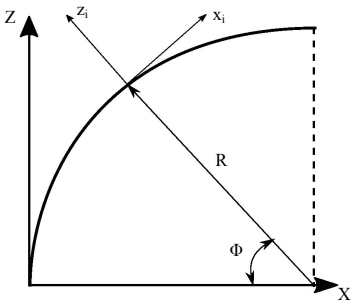

Fig. 3. Local Cartesian frame and curvilinear frame.

$$\mathbf{D}_s = \mathsf{diag}\left(AE, \beta^2 GA, \beta^2 GA, GI_x, EI_y, EI_z\right) \tag{17}$$

Now, introducing the stain mode matrix $\mathbf{\Phi}_1$ and the rigid body mode matrix $\mathbf{\Phi}_2$:

$$\mathbf{\Phi}_1 = \begin{pmatrix} 0 & -R^2\phi & R & 0 & 0 & 0 \\ 0 & 0 & 0 & 0 & R^2\phi & R\phi \\ R & R^2 & 0 & 0 & 0 & 0 \\ 0 & 0 & 0 & -R & 0 & 0 \\ 0 & R\phi & 0 & 0 & 0 & 0 \\ 0 & 0 & 0 & 0 & R & 0 \end{pmatrix} \tag{18}$$

$$\mathbf{\Phi}_2 = \begin{pmatrix} 1 & -s(\phi) & c(\phi) & 0 & 0 & 0 \\ 0 & 0 & 0 & 1 & c(\phi) & s(\phi) \\ 0 & c(\phi) & s(\phi) & 0 & 0 & 0 \\ 0 & 0 & 0 & 0 & -\frac{c(\phi)}{R} & -\frac{s(\phi)}{R} \\ -\frac{1}{R} & 0 & 0 & 0 & 0 & 0 \\ 0 & 0 & 0 & 0 & -\frac{s(\phi)}{R} & \frac{c(\phi)}{R} \end{pmatrix} \tag{19}$$

the local stiffness matrix $\mathbf{K}_p$ can be written as

$$\mathbf{K}_p = R\left(\phi_f - \phi_i\right) \mathbf{T}_2 \mathbf{A}_\phi^{-T} \mathbf{B}^T \mathbf{D}_s \mathbf{B} \mathbf{A}_\phi^{-1} \mathbf{T}_2^T \tag{20}$$

in which, denoting with ϕ_i and ϕ_f the initial and final angles of the curved beam and by introducing $\beta_i = \pi/2 - \phi_i$ and $\beta_f = \pi/2 - \phi_f$, we set the following matrices:

$$\mathbf{A}_\phi = \begin{pmatrix} \mathbf{\Phi}_1(\phi_i) & \mathbf{\Phi}_2(\phi_i) \\ \mathbf{\Phi}_1(\phi_f) & \mathbf{\Phi}_2(\phi_f) \end{pmatrix} \tag{21}$$

$$\mathbf{B} = \begin{pmatrix} 1 & 0 & 0 & 0 & 0 & 0 & 0 & 0 & 0 & 0 & 0 & 0 \\ 0 & 0 & 0 & 0 & 0 & 1 & 0 & 0 & 0 & 0 & 0 & 0 \\ 0 & 0 & 1 & 0 & 0 & 0 & 0 & 0 & 0 & 0 & 0 & 0 \\ 0 & 0 & 0 & 0 & 1 & 0 & 0 & 0 & 0 & 0 & 0 & 0 \\ 0 & 1 & 0 & 0 & 0 & 0 & 0 & 0 & 0 & 0 & 0 & 0 \\ 0 & 0 & 0 & 1 & 0 & 0 & 0 & 0 & 0 & 0 & 0 & 0 \end{pmatrix} \tag{22}$$

$$\mathbf{T}_2 = \begin{pmatrix} \mathbf{T}_{2i}(\beta_i) & \mathbf{O} & \mathbf{O} & \mathbf{O} \\ \mathbf{O} & \mathbf{T}_{2i}(\beta_i) & \mathbf{O} & \mathbf{O} \\ \mathbf{O} & \mathbf{O} & \mathbf{T}_{2i}(\beta_f) & \mathbf{O} \\ \mathbf{O} & \mathbf{O} & \mathbf{O} & \mathbf{T}_{2i}(\beta_f) \end{pmatrix} \tag{23}$$

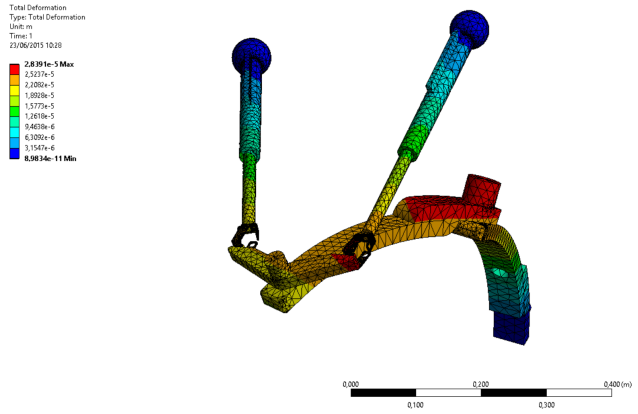

Fig. 4. Total deformations of the robot obtained using Ansys©. Pose parameters: $\{L_1, L_2, \theta_2\} = \{0.5195, 0.4984, 144.37°\}$.

The rotation matrix $\mathbf{T}_{2i}$ is a canonical y-axis rotation matrix used to express the local curvilinear frame rotated of the generic angle β with respect to the local Cartesian frame $X - Z$ of Fig. 3.

Once the stiffness matrix of the single curved beam is defined, one can build the generalized stiffness matrix of the limb. The first link, here referred to as proximal link, is linked to the BP by means of a revolute joint R_1. Recalling the *rigid body-flexible body* case, we can write $\mathbf{K}_a(\mathbf{h}^{R_1}, \mathbf{G}_{A_3}, \mathbf{K}_p)$, with obvious meaning of all symbols. Even in this case it would be convenient to put $\mathbf{G}_{A_3} = \mathbf{1}_6$.

The second revolute joint R_2 is actuated, therefore it is considered locked at a given configuration. The second curved beam, or distal link, is linked to the MP through the revolute joint R_3. Recalling the *flexible body-rigid body* case we write $\mathbf{K}_c(\mathbf{h}^{R_3}, \mathbf{G}_{B_3}, \mathbf{K}_d)$, in which $\mathbf{G}_{B_3} = \mathbf{1}$ because the node of the joint R_3 coincides with the reference node of the MP, and $\mathbf{K}_d$ is the stiffness matrix of the distal link. Notice that both $\mathbf{K}_p$ and $\mathbf{K}_d$ must be expressed into the global frame of reference.

C. Generalized Stiffness Matrix of the Robot

The generalized stiffness matrix of the robot can be found exploiting the results from the previous subsections. In order to improve the stiffness behaviour of the curved link, as already outlined in [19], we employ six FE to describe a single curved link. Seventeen nodes are first used to build the generalized stiffness matrix of the robot, then the fixed node of the BP is deleted by imposing boundary conditions, thereby obtaining a final model with sixteen nodes.

The final 96×96 generalized stiffness matrix is not shown for the sake of conciseness; further reading on the assembling method and other representative applications can be found in [22].

VI. Numerical results

In order to verify the proposed elastostatic method we applied a wrench at the point B_3. Hereafter, we will refer to the said wrench for the numerical results. Considering the interaction between the surgery tool and the skin we considered an axial force of 50 N acting along the translational direction of the end-effector and a transverse force of 5 N normal to the end-effector. A torque of 2.7 Nm, along the axis Y_4 that lies on the plane of the MP and normal to Z_4, has been also taken into account considering that tissue interaction forces induce moments on the MP.

TABLE II. Comparison to Ansys results: statics.

	s	ξ
Model	6.7308E-5	2.632E-4
Ansys	2.1510E-5	6.129E-5

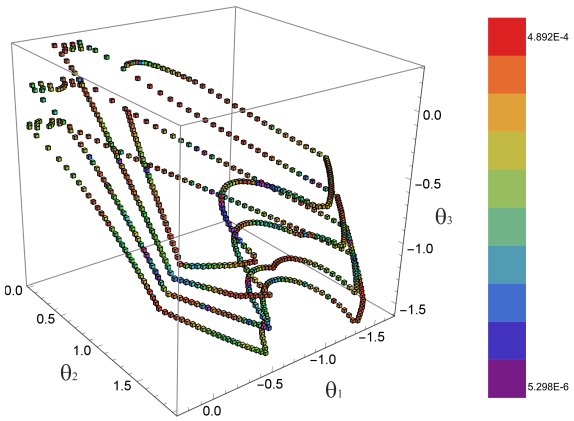

Fig. 5. Positioning error along the boundaries of workspaces with different constant orientations within the range $[-60°, 60°]$ expressed in the joint space of the three revolute joints. Values of s, expressed in [m], are reported on the legend bar.

In order to validate the model we performed a static analysis using Ansys©. For our purposes we measured the displacement s and the rotation angle ξ of the MP, due to the deformation, following the approach proposed in [23]. The total deformations coming from the application of the static wrench, discussed above, are reported in Fig. 4 and compared to the proposed model results in Tab. II. Some discrepancies occur as we compare a three dimensional model with tetrahedral FE with a numerical model based on beams. Besides, joint stiffness is not considered into the proposed model as well as MP flexibility. Moreover, structural elements as ribs, holes and fillets modify the global stiffness of the robot and are difficult to be taken into account in a model with simplified geometries.

We calculated the error positioning analysis along the boundaries of workspaces with different constant orientations within the range $[-60°, 60°]$. A constant orientation of the MP means that the angle ψ between the projection of the axis O_4X_4 on the plane OXY and the axis OX is kept constant. We refer the reader to [16] for more details on the robot's workspace.

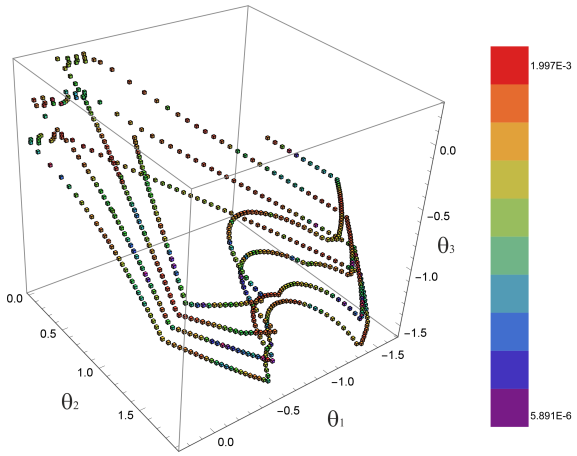

Fig. 6. Orienting error along the boundaries of workspaces with different constant orientations within the range $[-60°, 60°]$ expressed in the joint space of the three revolute joints. Values of ξ, expressed in $[rad]$, are reported on the legend bar.

Based on data reported in medical literature [24], we have imposed a maximum error of 0.5 [mm] for the displacement s and a maximum error of 0.002 [rad] for the rotation angle ξ. These values change depending on the applications but position sensors are usually required to measure the tip of a surgical device in the range of 1–2 [mm] and orientation ranging from 0.5 to 2 [degrees]. We decided to go below these values because we consider only the robot's structure deformation without including the tip deflection.

The two Figures 5&6 show the errors, coming from the application of the static wrench, that are above the limit values. Each point of the boundaries is detected by a small colored cube in which the color indicates the positioning error, either linear or angular, following the color map of the legend bar. Some voids reveals points of the boundary in which the errors are above the limit values that we imposed.

To improve the performance of the robot, limiting the deformations of its end-effector, we carried out a sensitivity analysis considering changes in geometric parameters. In particular, we want to analyse how the positioning errors change when we modify the positions of the limb's attachment points to the BP or MP. For our purposes let us consider an arbitrary pose expressed in the joint space of the three revolute joints $\{\theta_1, \theta_2, \theta_3\} = \{-0.568, 1.588, -1.136\}$. Now let us consider how the errors s and ξ are influenced changing the x-coordinates x_A and x_B of the attachment points to the BP or MP. Figure 7 shows that the errors increase when the parameter x_A increases but they decrease when x_B increases. This tradeoff reveals that it is possible to increase the performance using an optimization procedure in which geometric parameters are considered optimization variables.

Making use of the results outlined in Fig. 7 we performed an analysis on a modified version with $x_A = 0.1$ [m] and

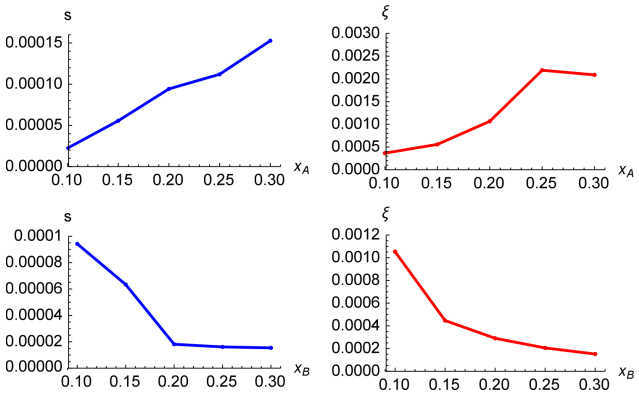

Fig. 7. Positioning and orienting errors vs. geometric parameters. Values of s are expressed in [m]; those of ξ are in $[rad]$; x_A and x_B are in [m].

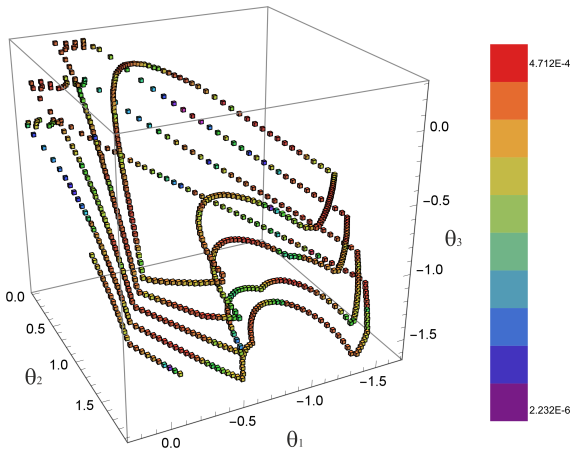

Fig. 8. Positioning error of the modified version along the boundaries of workspaces with different constant orientations within the range $[-60°, 60°]$ expressed in the joint space of the three revolute joints. Values of s, expressed in [m], are reported on the legend bar.

$x_B = 0.3$ [m]. As expected, the errors due to deformations under the same static wrench decrease compared to the original version. Figures 8&9 show the positioning and orienting errors of the modified version calculated along the same boundaries of Figs. 5&6. The reader may notice a greater number of points than the original version as well as increased performance all over the boundaries of workspaces. In Table III we summarized the number of points N_s and N_ξ that are above the limit values introduced above; the mean values $\overline{s}$ and $\overline{\xi}$; and the standard deviations σ_s and σ_ξ of s and ξ, respectively. We observe great dispersions of data comparable with the mean values for both the modified and original versions. For future developments an optimized structure should be aimed to reduce error dispersion and mean values at the same time.

VII. Conclusions

The elastostatic model of a novel hybrid robot for minimally invasive surgery has been described. Inverse and

TABLE III. Performance evaluation: original version vs. modified version.

	N_s	N_ξ	$\overline{s}$	$\overline{\xi}$	σ_s	σ_ξ
Original	629	604	1.101E-4	4.672E-4	1.121E-4	4.209E-4
Modified	670	667	7.009E-5	3.099E-4	7.316E-5	3.125E-4

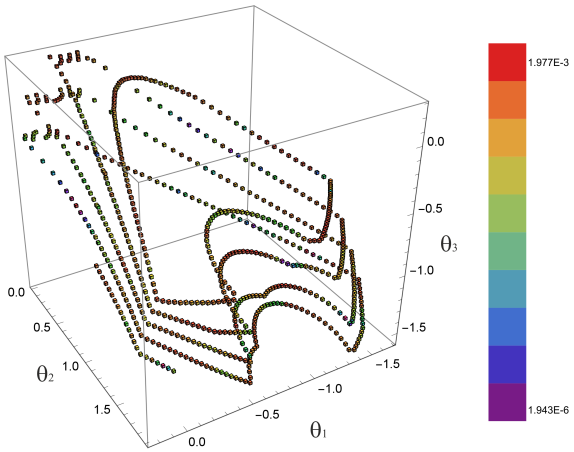

Fig. 9. Orienting error of the modified version along the boundaries of workspaces with different constant orientations within the range $[-60°, 60°]$ expressed in the joint space of the three revolute joints. Values of ξ, expressed in $[rad]$, are reported on the legend bar.

forward kinematics have been briefly recalled as necessary for the elastostatic analysis. The latter is based on linearity and small displacements assumptions. Links composing the structure have been considered flexible bodies while the two platforms have been modeled as rigid bodies. Besides, we employed curved two-node Timoshenko's beams, with constant strain fields, to achieve the symbolic stiffness matrix of curved links composing the 3R limb of the robot. Two cases describing the coupling of rigid and flexible bodies through joints have been recalled from [18] to derive local stiffness matrices. The latter have been combined to obtain the limb stiffness matrices of the robot.

Statics analysis has been performed and compared to commercial FE software for validation. Then, positioning and orienting errors have been evaluated for the boundaries of workspaces with different constant orientations by applying a wrench simulating the interaction between the skin and the surgical instrument. Results revealed that the deformations are above the limit values imposed for some points of the boundary.

Some feasible extensions to optimization techniques are finally included to analyse the sensitivity of the deformation errors to some geometric parameters. Future developments will pertain to optimization methods extended to the combined use of geometrical and structural parameters as optimization variables.

References

[1] Taylor R.H., and Stoianovici D. Medical robotics in computer-integrated surgery, *IEEE Transactions on Robotics and Automation*, vol. 19, No. 5, pp. 765–781, 2003.

[2] Kuo C-H., and Dai J. S. Robotics for minimally invasive surgery: a historical review from the perspective of kinematics, In *International Symposium on History of Machines, Springer Science+Business Media B.V.*, pp. 337–354, 2009.

[3] Guthart G., and Salisbury J.K. The Intuitive telesurgery system: overview and applications. *IEEE Int. Conf. on Robotics and Automation*, pp. 618–621, 2000.

[4] Rosen J., Brown J.,Chang L., Barreca M., Sinanan M., and Hannaford, B. The BlueDRAGON - a system for measuring the kinematics and the dynamics of minimally invasive surgical tools in-vivo. In *Proc. IEEE International Conference on Robotics and Automation*, pp.1876–1881, Washington, USA, 2002.

[5] Lum M.J.H., Rosen J., Sinanan M., Hannaford B. Kinematic optimization of a spherical mechanism for a minimally invasive surgical robot. In *Proc. IEEE International Conference on Robotics and Automation*, New Orleans, La, May 2004.

[6] Schena, B. M. Center robotic arm with five-bar spherical linkage for endoscopic camera. *United State Patent No. US8167873B2*, 2007.

[7] Zemiti N., Morel G., Ortmaier T., and Bonnet N. Mechatronic design of a new robot for force control in minimally invasive surgery. *IEEE/ASME Transactions on Mechatronics*, Vol. 12, No. 2, pp. 143–153, 2007.

[8] Khan M. A., Zoppi, M. and Molfino R. 4-DOF Parallel Architecture for Laparoscopic Surgery. *Advances in Robot Kinematics: Analysis and Design, J. Lenarcic and P. Wenger (Eds), Springer-Verlag*, pp. 119–126, 2008.

[9] Li T. and Payandeh S. Design of Spherical Parallel Mechanisms for application to Laparoscopic Surgery. *Robotica*, vol. 20, p. 133–138, 2002.

[10] Sabater-Navarro J.M. et al. A simple and compact parallel robotic wrist for laparoscopy. *The Fourth IEEE RAS/EMBS International Conference on Biomedical Robotics and Biomechatronics*, pp. 835–840, Roma, Italy, June 24-27, 2012.

[11] Kuo C.-H., Dai J.S. Kinematics of a fully-decoupled remote center-of-motion parallel manipulator for minimally invasive surgery. *ASME J. Med. Devices*, 6 (2), pp. 021008 (1–12), 2012.

[12] Dalvand M. M. and Shirinzadeh B. Remote Centre-of-Motion Control Algorithms of 6-RRCRR Parallel Robot Assisted Surgery System (PRAMiSS). *IEEE International Conference on Robotics and Automation (ICRA)*, pp. 3401–3406, Saint Paul, Minnesota, USA, May 14-18, 2012.

[13] Taniguchi K. et al. Design of a novel wearable laparoscope manipulator: SMART (Synthetic Muscle Actuator based Robotic Technology). *International Journal of Assisted Radiology and Surgery*, 1 (suppl. 1), pp. 213–215, 2006.

[14] Sima'an N., Glozman D. and Shoham M. Design considerations of new six degrees-of-freedom parallel robots. *Proc. IEEE International Conference on Robotics and Automation*, pp. 1327–1333, Leuven, Belgium, May 1998.

[15] Pisla D., Gherman B., Vaida C. and Plitea N. Kinematic modelling of a 5-DOF hybrid parallel robot for laparoscopic surgery. *Robotica*, Vol. 30, (07), pp. 1095–1107, 2012.

[16] Tanev T.K. Minimally-invasive-surgery parallel robot with non-identical limbs. In *Proc. 10th IEEE/ASME International Conference on Mechatronic and Embedded Systems and Applications (MESA2014)*, DOI:10.1109/MESA.2014.6935558, Senigallia, Italy, September 10-12, 2014.

[17] Tanev T.K. Singularity analysis of a novel minimally-invasive-surgery hybrid robot using geometric algebra. In *4th International Workshop on Medical and Service Robots (MESROB2015)*, Nantes, France, July 8-10, 2015 (to appear).

[18] Cammarata A. On the stiffness analysis and elastodynamics of parallel kinematic machines. In *Serial and Parallel Robot Manipulators: Kinematic Dynamics and Control*, In-Tech, Rijeka, Croatia, 2012.
[19] Choi J-K., and Lim J-K. General curved beam elements based on the assumed strain fields. In *Computers & Structures* 55(3):379–386, 1995.
[20] Prathap G., and Babu C.R. An isoparametric quadratic thick curved beam element. In *International Journal for Numerical Methods in Engineering* 23(9):1583–1600, 1986.
[21] Palaninathan, R., and Chandrasekharan, P.S. Curved beam element stiffness matrix formulation. In *Computers & structures* 21(4): 663–669, 1985.
[22] Cammarata, A. and Sinatra, R. Elastodynamic optimization of a 3T1R parallel manipulator. In *Mechanism and Machine Theory* 73: 184–196, 2014.
[23] Palmieri, G., On the positioning error of a 2 DOF spherical parallel wrist with flexible links and joints - a FEM approach. In press on *Mechanical Sciences*.
[24] Glossop, N., Localization and tracking technologies for medical robotics. In *Medical Robotics*, 41–58. Woodhead Publishing Series in Biomaterials, 2012.